Single-line-extracted pure rotational Raman lidar to measure atmospheric temperature and aerosol profiles

MIAO WENG,^{1,2,3} FAN YI,^{1,2,3,*} FUCHAO LIU,^{1,2,3} YUNPENG ZHANG,^{1,2,3} AND XIANGLIANG PAN^{1,2,3}

Abstract: We have built a pure rotational Raman (PRR) lidar system that effectively detects two isolated N₂ molecule PRR line signals and elastic backscatter signals. This system enables all-day temperature profiles to be accurately obtained without calibration, according to the simple two-parameter functional relationship between the temperature and ratio of the two PRR line signals. Based on the derived temperature profiles, the aerosol backscatter and extinction profiles can be further determined strictly from one measured PRR line signal and elastic backscatter signal without additional assumptions. The two aerosol parameters and resultant lidar ratio provide strict standards for the lidar measurements of aerosol.

© 2018 Optical Society of America under the terms of the OSA Open Access Publishing Agreement

1. Introduction

Accurate and high-resolution measurements of atmospheric temperature are required to identify meteorological processes and climate trend. Vertical temperature profiles are usually acquired by routinely launched radiosondes (typically twice a day). Although such routine radiosonde temperature profiles have a high accuracy and good altitude resolution, their low time resolution makes it unlikely to register some fast weather processes. Pure rotational Raman (PRR) lidar can overcome this drawback to obtain high time-resolution temperature profiles throughout the troposphere [1-4]. The PRR lidar technique is based on a fact that under local thermodynamic equilibrium conditions, the signal intensity ratio of two individual PRR lines has validly a simple two-parameter temperature dependence defined by the Boltzmann distribution and is independent of atmospheric transmission and altitude. However, because the line spacing of the PRR spectrum (composed of N₂ and O₂ PRR lines) is uneven and mostly narrow, and the available spectral extraction devices (interference filter, grating polychromator and Fabry-Perot interferometer as a comb-filter) have a limited bandwidth, each rotational Raman channel in the existing PRR lidars has to extract several adjacent PRR lines of both N₂ and O₂ rather than a single one [1,4-6]. Then the signal ratio becomes a complicated function of temperature so that the strict solution of temperature is unavailable. In this case, a calibration function with an argument of second-order polynomial of inverse temperature is introduced to approximately represent the temperature dependence of the signal ratio [7]. Although the simulations indicate that this calibration function can approaches well the theoretical result of the signal ratio for sampling two multiple-line portions of the PRR spectrum [5,7], the approximate expression for the principle of the PRR temperature measurement induces a systematic error after all. In addition, the introduced calibration constants also lack a clear-cut connection with the result of the Raman scattering theory and lidar system parameters. Therefore, to ensure reliable temperature measurement, it is significant to develop a single-line-extracted PRR lidar (which makes the basic principle of the PRR temperature measurement valid).

¹School of Electronic Information, Wuhan University, Wuhan 430072, China

²Key Laboratory of Geospace Environment and Geodesy, Ministry of Education, Wuhan, China

³State Observatory for Atmospheric Remote Sensing, Wuhan, China

^{*}yf@whu.edu.cn

Lidar profiling of aerosol optical properties has provided significant observational bases for understanding a role of atmospheric aerosols in the Earth's climate system and in cloud and precipitation processes [8-13]. Nevertheless, the determination of aerosol optical properties needs to introduce additional assumptions. It is well known that the data retrieval of the elastic lidar return suffers from the fact that the two unknowns (the particle backscatter coefficient and particle extinction coefficient) must be determined from only one measured quantity (one equation). Thus an additional assumption is introduced to settle this problem. Fernald developed an algorithm to derive the two unknowns by assuming that the ratio of aerosol extinction coefficient to backscatter coefficient (lidar ratio) was a given constant value [14]. This lidar ratio assumption is usually not true in the actual atmosphere. An vibration-rotational Raman lidar that detects both elastically backscattered signal from air molecules and aerosols and Raman backscattered signal by N₂ (or O₂) molecules can yield two lidar equations. The two equations however include three unknown aerosol optical parameters, i.e., particle extinction coefficients at the transmitted wavelength and Ramanshifted wavelength as well as particle backscatter coefficient at the transmitted wavelength. Then an assumed wavelength dependence (i.e., the Ångström relationship) on the particle extinction coefficient must be introduced to obtain the solutions for the aerosol optical properties at the transmitted wavelength [15]. The additional assumption apparently results in quantitative uncertainties in estimated particle backscatter and extinction coefficients.

We have recently found two pairs of individual N_2 molecule PRR lines (anti-Stokes PRR lines J=6 and 16, and Stokes PRR lines J=4 and 14) from the calculated PRR spectra of N_2 and O_2 that are isolable or extractable by using a combination of commercially-available interference filter and Fabry-Perot interferometer (FPI). In light of this result, we have designed and built a single-line-extracted pure rotational Raman (PRR) lidar system that effectively detects two isolated N_2 molecule PRR line signals (anti-Stokes PRR lines J=6 and 16) and elastic backscatter signal. This system enables all-day temperature profiles to be accurately determined from the simple two-parameter temperature dependence of the ratio of the two PRR line signals without data calibration from other instrument (temperature) measurement. Based on the derived temperature profiles, the aerosol backscatter and extinction profiles can be further determined strictly from one measured PRR line signal and elastic backscatter signal without additional assumptions (e.g., lidar ratio or Ångström relationship). The two aerosol parameters as well as resultant lidar ratio provide quantitatively strict standards for the lidar measurements of aerosol.

2. Measurement principle and statistical error

The differential backscatter cross section for single lines of the gas species i (N₂ or O₂) in the rotational quantum state J at the absolute temperature T is given by [5,7]:

$$\sigma_{i,J}(T) = \frac{112\pi^4}{15} \frac{hcB_i}{(2I_i + 1)^2 kT} g_i(J) X(J) \left(v_0 + \Delta v_i(J)\right)^4 \frac{\gamma_i^2}{(4\pi\varepsilon_0)^2} \exp\left[-\frac{E_i(J)}{kT}\right]$$
(1)

where h is Planck's constant, c is the velocity of light, B_i is the rotational constant ($B_{N_2} = 1.98957cm^{-1}$ and $B_{O_2} = 1.43768cm^{-1}$), I_i is the nuclear spin quantum number ($I_{N_2} = 1$ and $I_{O_2} = 0$), k is the Boltzmann constant, $g_i(J)$ is a statistical weight factor whose value is 6 and 3 respectively for even- and odd- J N₂ lines, and 0 and 1 respectively for even- and odd- J O₂ lines, v_0 is the emitted frequency (expressed in cm⁻¹). $E_i(J)$ is the rotational energy which takes the form:

$$E_i(J) = \left[B_i J(J+1) - D_i J^2 (J+1)^2 \right] hc, \quad J = 0, 1, 2...$$
 (2)

where D_i is the centrifugal distortion constant ($D_{N_2} = 5.76 \times 10^{-6} \, cm^{-1}$ and $D_{O_2} = 4.85 \times 10^{-6} \, cm^{-1}$). $\Delta V_i(J)$ is the Raman shift which can be calculated with:

$$\Delta V_i(J) = \begin{cases} -B_i 2(2J+3) + D_i \left[3(2J+3) + (2J+3)^3 \right], & J = 0, 1, 2...(Stokes) \\ B_i 2(2J-1) - D_i \left[3(2J-1) + (2J-1)^3 \right], & J = 2, 3, 4...(antiStokes) \end{cases}$$
(3)

The factor X(T) is given by

$$X(J) = \begin{cases} \frac{(J+1)(J+2)}{2J+3} & (Stokes) \\ \frac{J(J-1)}{2J-1} & (antiStokes) \end{cases}$$
 (4)

The combined expression of the anisotropy of the polarizability γ_i and the permittivity of vacuum ε_0 has the value [16]:

$$\frac{\gamma_i^2}{(4\pi\epsilon_0)^2} = \begin{cases} 0.51 \times 10^{-60} \left(for \ \gamma_{N_2}^2 \ in \ unit \ of \ m^6 \right) \\ 1.27 \times 10^{-60} \left(for \ \gamma_{O_2}^2 \ in \ unit \ of \ m^6 \right) \end{cases}$$
 (5)

The N_2 and O_2 PRR spectra can be calculated with Eq. (1) for a given laser wavelength and temperature. Figure 1 shows the calculated result for a laser wavelength of 532.237 nm and temperature T = 300K. As seen from Fig. 1, for the anti-Stokes branch, the two N_2 PRR lines with J = 6 and 16 (marked with thick red line) have distances larger than 0.14 nm from adjacent O_2 PRR lines. For the Stokes branch, the similar feature can be seen from the two N_2 PRR lines with J = 4 and 14 (not shown here). Each of the two pair of the individual N_2 PRR lines (anti-Stokes PRR lines J = 6 and 16, and Stokes PRR lines J = 4 and 14) is isolable or extractable by using a combination of commercially-available interference filter (IF) and Fabry-Perot interferometer (FPI) (Transmittances of IF and FPI are shown in Fig. 1). Thus we have designed and built a single-line-extracted PRR lidar with the anti-Stokes PRR lines J = 6 and 16. The photon count detected in each single-line-extracted PRR channel can be expressed as [5,17]:

$$N_{J}(z) = \frac{C_{J}}{z^{2}} n(z) \sigma_{N_{2,J}}(T) \exp\left\{-\int_{0}^{z} \left[\alpha_{a,v_{0}}(z') + \alpha_{m,v_{0}}(z') + \alpha_{a,v_{J}}(z') + \alpha_{m,v_{J}}(z')\right] dz'\right\}, \quad J = 6 \quad and \quad 16$$
(6)

where C_J is the system factor for the channel J that is proportional to the transmitted laser pulse energy and the overall channel efficiency (in the channel J), n(z) is the number density of the atmospheric molecules, $\alpha(z)$ is the distance-dependent extinction coefficient with subscripts a and m denoting particle and molecule contributions respectively, v_J Raman-shifted frequency. Note that the aerosol and molecular extinctions at frequency $v_{J=6}$ closely approach in quantity that at frequency $v_{J=16}$ and $[v_0 + \Delta v_{N_2}(J=16)]^4/[v_0 + \Delta v_{N_2}(J=6)]^4 \approx 1$. In terms of Eqs. (1)-(6), the ratio Q(T) of the lidar-detected photon counts for the two individual N_2 PRR line channels with J=6 and 16 has the following simple temperature dependence:

$$Q(T) = \frac{N_{J=16}(z)}{N_{J=6}(z)} = \exp\left(\frac{a}{T} + b\right)$$
(7)

with

$$a = \frac{E_{N_2}(J=6) - E_{N_2}(J=16)}{k} = \frac{(-230B_{N_2} + 72220D_{N_2})hc}{k} = -658.38K$$
 (8)

$$b = \ln\left(\frac{C_{J=16}}{C_{J=6}}\right) + \ln\left[\frac{X(J=16)}{X(J=6)}\right] = \ln\left(\frac{C_{J=16}}{C_{J=6}}\right) + 1.04$$
(9)

The value of 1.04 in Eq. (9) is obtained by substituting J = 16 and J = 6 into $\ln \left[\frac{X(J=16)}{X(J=6)} \right]$ (with $X(J) = \frac{J(J-1)}{2J-1}$). Obviously, the parameter a is a known constant

that is independent of the lidar system parameters. The parameter b depends on the logarithm of the ratio $C_{J=16}/C_{J=6}$. The ratio $C_{J=16}/C_{J=6}$ is equivalent to the ratio of the overall channel efficiencies for J=16 and J=6 given that the laser pulse energy and telescope area are invariable. Its value can be estimated by collecting the lidar signals based on the emission of a dye laser with a tunable range covering the interested PRR wavelengths. After the parameter b is obtained via measuring $C_{J=16}/C_{J=6}$, the distance-dependent atmospheric temperature can be determined from Eq. (7). Hence the single-line-extracted PRR lidar can retrieve temperature profiles without data calibration from other instrument measurement (e.g., local radiosonde). If the accompanying radiosondes are available, a comparison between the calibrated constants a and b, and their theoretical and measured results provides a criterion for validating the accomplishment of the single-line-extracted PRR lidar.

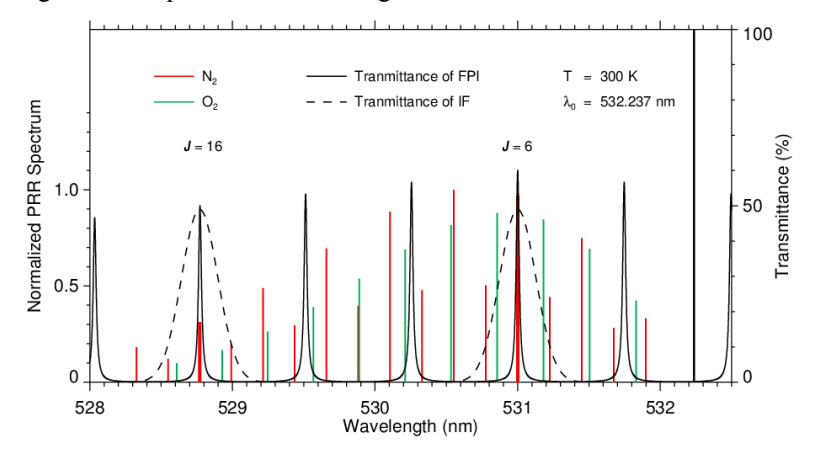


Fig. 1. Anti-Stokes pure rotational Raman spectrum of a mixture of N_2 (red) and O_2 (green) calculated for a laser wavelength of 532.237 nm and a temperature of 300 K. The relative volume abundances are respectively 0.78 for N_2 and 0.21 for O_2 . Note that the two N_2 PRR lines with J=6 and 16 (marked with thick red line) have distances larger than 0.14 nm from adjacent O_2 PRR lines. They are isolable by using a combination of commercially-available interference filter (IF) and Fabry-Perot interferometer (FPI). The transmittances of IF (dashed black) and FPI (solid black) are also plotted.

In order to obtain the aerosol optical properties, an elastic channel is added to the single-line-extracted PRR lidar. The photon count detected in the elastic channel is given by [15,18]:

$$N_{\nu_0}(z) = \frac{C_{\nu_0}}{z^2} \Big(\beta_{a,\nu_0}(z) + \beta_{m,\nu_0}(z) \Big) \exp \Big\{ -2 \int_0^z \Big[\alpha_{a,\nu_0}(z') + \alpha_{m,\nu_0}(z') \Big] dz' \Big\}$$
(10)

where C_{ν_0} is the system factor for the elastic channel ν_0 that is proportional to the transmitted laser pulse energy and the overall channel efficiency (in the elastic channel), $\beta_{a,\nu_0}(z)$ and $\beta_{m,\nu_0}(z)$ denote the backscatter coefficients respectively for aerosol (subscript a) and air molecules (subscript m). In Eq. (10), the molecular backscatter and extinction coefficients $\beta_{m,\nu_0}(z)$ and $\alpha_{m,\nu_0}(z)$, as known quantities, can be calculated from local radiosonde data, while the corresponding quantities for aerosol particles $\beta_{a,\nu_0}(z)$ and $\alpha_{a,\nu_0}(z)$ are two unknowns to be determined. Given a fact that the atmospheric transmission is nearly constant within the PRR spectrum (the wavelength difference between the J=6 line signal and the elastic signal is less than 1.2 nm), combining Eq. (6) for J=6 and Eq. (10) yields a new expression for the particle backscatter coefficient $\beta_{a,\nu_0}(z)$ and backscatter ratio R(z):

$$\beta_{a}(z) = \beta_{m}(z) \frac{T(z_{0}) \exp\left[-\frac{B_{N_{2}}hc}{kT(z)}J(J+1)\right]}{T(z) \exp\left[-\frac{B_{N_{2}}hc}{kT(z_{0})}J(J+1)\right]} \frac{N_{v_{0}}(z)N_{J}(z_{0})}{N_{v_{0}}(z_{0})N_{J}(z)} - \beta_{m}(z)$$

$$(11)$$

$$R(z) = \frac{\beta_{a}(z) + \beta_{m}(z)}{\beta_{m}(z)} = \frac{T(z_{0}) \exp\left[-\frac{B_{N_{2}}hc}{kT(z)}J(J+1)\right]}{T(z) \exp\left[-\frac{B_{N_{2}}hc}{kT(z_{0})}J(J+1)\right]} \frac{N_{\nu_{0}}(z)N_{J}(z_{0})}{N_{\nu_{0}}(z_{0})N_{J}(z)}$$
(12)

where $\beta_a(z)$ and $\beta_m(z)$ denote respectively $\beta_{a,v_0}(z)$ and $\beta_{m,v_0}(z)$ for simplicity, z_0 is a reference height where the particle backscatter coefficient is negligible ($\beta_a(z_0) \approx 0$) compared to the molecular backscatter value, T(z) is the atmospheric temperature retrieved antecedently from Eq. (7), the rotational quantum number J=6, which has a relatively higher line intensity. Equations (11) and (12) indicate that for the single-line-extracted PRR lidar with two N₂ PRR line channels and one elastic channel, the particle backscatter coefficient $\beta_a(z)$ (or backscatter ratio R(z)) can be strictly determined from the previously-retrieved atmospheric temperature T(z), the signal intensities in one N₂ PRR line channel and elastic channel. Equation (11) provides so far a unique strict solution to the particle backscatter coefficient without introducing additional assumptions. By inserting the derived particle backscatter coefficient $\beta_a(z)$ in Eq. (11), the particle extinction coefficient can be obtained further from the following expression:

$$\alpha_a(z) = \frac{1}{2} \frac{d}{dz} \left[\ln \frac{\beta_a(z) + \beta_m(z)}{N_{\nu_0}(z)z^2} \right] - \alpha_m(z)$$
(13)

where $\alpha_a(z)$ and $\alpha_m(z)$ denote respectively $\alpha_{a,\nu_0}(z)$ and $\alpha_{m,\nu_0}(z)$ for simplicity. Equation (13) represents also a strict solution of the aerosol extinction coefficient without additional

assumptions. The lidar ratio is calculated according to its definition from the profiles of the obtained aerosol extinction coefficient and backscatter coefficient.

The statistical error for the temperature and aerosol measurements needs be considered as a measure of measurement precision. Assuming that the background-subtracted photon counts $N_{J=16}(z)$, $N_{J=6}(z)$ and $N_{\nu_0}(z)$ are statistically independent and each follows the Poisson distribution [19], the $1-\sigma$ uncertainty of the measured photon count N is given by

$$\Delta N = \sqrt{N} \tag{14}$$

Combining Eqs. (7) and (14), the uncertainty of the current temperature measurements ΔT can be written as [7]:

$$\Delta T = \frac{\partial T}{\partial Q} \Delta Q = \frac{\partial T}{\partial Q} Q \sqrt{\frac{1}{N_{J=6}} + \frac{1}{N_{J=16}}}$$
(15)

After obtaining the uncertainty of the temperature measurements, the uncertainty of the backscatter ratio R(z) is given by:

$$\Delta R = R \left[\frac{1}{T(z_0)^2} (1 - \frac{C_0}{T(z_0)})^2 (\Delta T(z_0))^2 + \frac{1}{T(z)^2} (1 - \frac{C_0}{T(z)})^2 (\Delta T(z))^2 + \frac{1}{N_{\nu_0}(z)} + \frac{1}{N_{\nu_0}(z_0)} + \frac{1}{N_{J=6}(z)} + \frac{1}{N_{J=6}(z_0)} \right]^{1/2}$$
(16)

where $C_0 = \frac{B_0 hc}{k} J(J+1)$. In terms of Eq. (12), the uncertainty of the particle backscatter coefficient is expressed as:

$$\Delta \beta_a = \beta_m \Delta R \tag{17}$$

The uncertainty of the particle extinction coefficient can be derived from Eqs. (13)-(17). It is not given here because of its complexity.

3. System setup

In light of the concept description above, Fig. 2 presents an optical layout of the single-lineextracted PRR lidar. The lidar transmitter employs an injection-seeded frequency-doubled Nd: YAG laser that yields a 532,237-nm laser beam of ~800 mJ per pulse with a repetition rate of 30 Hz and linewidth of <0.006 cm-1. An 8 × beam expander is used to reduce the radiant flux density and divergence of the output laser beam. The expanded laser beam is guided into the atmosphere zenithward by an electronically-steerable reflecting mirror (RM1). At receiver side, the backscattered photons are collected by a 200-mm Cassegrain telescope. A field-stop iris on the focal plane of the telescope is used to set the lidar field of view (~0.4 mrad). After the iris, the collected signal light is redirected by RM2 and collimated by lens L4 and then incident on a cube beam splitter (BS1). The BS1 separate the incident signal light into two equal parts: one part is transmitted to the second cube beam splitter (BS2), another part is reflected into the high-quantum-number PRR channel. In the high- J channel, the combined interference filter IF2 and Fabry-Perot interferometer FPI2 are set to transmit the anti-Stokes N_2 PRR line with J = 16. The signal light exiting the FPI2 is focused by a lens (L2) and detected by a photomultiplier tube (PMT2). The IF2 consists of two identical interference filters with each having 0.3-nm bandwidth, ~70% peak transmission at 528.770 nm and a rejection ratio of >3 orders of magnitude to signals out of band. With delicate

temperature control and angle adjustment, the FPI2 can accurately extract the anti-Stokes N_2 PRR J=16 line (corresponding to the wavelength of 528.770 nm). The FPI2 has a peak transmission of ~50% at 528.770 nm and a bandwidth (FWHM) of ~30 pm. It provides a suppression by more than 2 orders of magnitude to the elastic signal around 532.237 nm, and also suppression by more than 1.5 orders of magnitude to the adjacent O_2 PRR lines (i.e., the O_2 PRR J=21 line at the wavelength of 528.928 and O_2 PRR J=23 line at 528.609 nm). The suppressions to both the elastic signal and the adjacent O_2 PRR lines ensure that the single anti-Stokes N_2 PRR J=16 line can be effectively isolated.

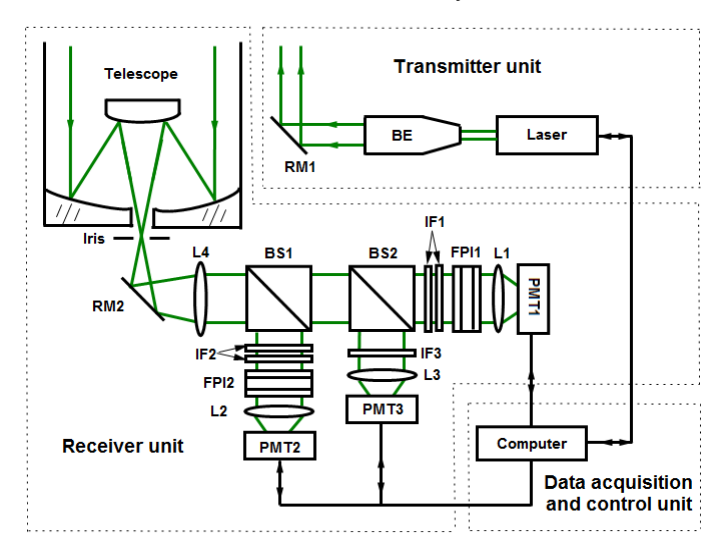


Fig. 2. Optical layout of Wuhan University single-line-extracted PRR lidar for measuring atmospheric temperature and aerosol optical properties. BE, beam expander; RM, reflecting mirror; BS, beam splitter; L, lens; IF, interference filter; FPI, Fabry-Perot interferometer; PMT, photo-multiplier tube.

The BS2 divides the BS1-transmitted light into the low-quantum-number PRR channel and the elastic channel. This low- J PRR channel performs the extraction of the single anti-Stokes N_2 PRR J = 6 line at the wavelength of 531.000 nm with the combined interference filter IF1 and Fabry-Perot interferometer FPI1. The IF1 is also made up of two identical interference filters (each has 0.3-nm bandwidth, ~70% peak transmission at 531.000 nm and a rejection ratio of >3 orders of magnitude to signals out of band). The FPI1 has a peak transmission of ~60% at 531.000 nm and a bandwidth (FWHM) of ~30 pm. It produces a suppression by more than 2 orders of magnitude to the elastic signal around 532.237 nm, and also suppression by more than 1.5 orders of magnitude to the adjacent O₂ PRR lines (i.e., the O_2 PRR J = 7 line at the wavelength of 531.180 nm and O_2 PRR J = 9 line at 530.857 nm). Therefore the combined IF1 and FPI1 effectively transmit the single anti-Stokes N₂ PRR J = 6 line at the wavelength of 531.000 nm. The signal light exiting the FPI1 is focused on the photomultiplier tube PMT1 by lens L1. In the elastic channel, the BS2-reflected light goes through the interference filter IF3 which has a 0.3-nm bandwidth, ~80% peak transmission at 532.237 nm and a rejection ratio of >4 orders of magnitude to signals out of band, and then is focused on the photomultiplier tube PMT3 by lens L3. Thus the single-line-extracted PRR lidar has three channels. The signal at each channel is acquired by a PC-controlled transient digitizer in the data acquisition and control unit. The raw lidar data have an altitude resolution of 7.5 m and a time resolution of 60 s.

4. FPI adjustment and system calibration

The FPI installation requires a fine adjustment under clear-sky conditions to determine its working angle where the single anti-Stokes N_2 PRR line can be effectively extracted. For this purpose, each FPI in this lidar system was put on a finely adjustable mount. A dye (Coumarin 535) laser pumped by a tripled Nd:YAG laser was temporarily employed as a lidar transmitter during the FPI adjustment. The dye laser (NarrowScanK, Radiant Dyes Laser, Acc. GmbH) has a tunable range from 525 to 535 nm and a linewidth of ~3 pm. Its output wavelength was monitored by a pulsed wavemeter (HighFinesse, WS7). The dye laser beam was directed vertically into the atmosphere by a computer-controlled gimbal-mounted mirror. The backscattered light was collected and delivered to the three different channels as shown in Fig. 2. Firstly, under the condition that the output wavelength of the dye laser was set to the anti-Stokes N_2 PRR J=6 line (531.000 nm), we determined the working angle of the FPI1 by finely adjusting the FPI1 mount. When the FPI1 mount was adjusted to a position where the intensity of the PMT1 output signal reached its maximum, the FPI1 adjustment was accomplished and the mount-data-derived angle was set to the working angle. It has a value of ~8° which is close to the designed value.

The single-line-extraction performance of the anti-Stokes N_2 PRR J=6 channel can be examined also by the current tunable dye laser. We measured the PMT1 output signals as the dye laser was respectively tuned to the anti-Stokes N_2 PRR J=6 line and its neighbouring O_2 and N_2 lines (i.e., the anti-Stokes O_2 PRR J=7 and J=9 lines, as well as the anti-Stokes N_2 PRR J = 5 and J = 7 lines). The dye laser had a pulse energy of ~6 mJ at these wavelengths and each signal was integrated over one minute. Since the wavelength tuning range was only ~0.44 nm and the tuning/measurement procedure was carried out in a period of ~6 min, both the output energy of the dye laser and the atmospheric transmittance were nearly constant. Figure 3(a) shows the normalized PMT1 signal intensity for the laser emissions at the anti-Stokes N_2 PRR J = 6 line and the four O_2 and N_2 lines close to it. The normalization factor is the signal intensity value at the anti-Stokes N_2 PRR J = 6 line. Hence the normalized intensities represents the relative transmittance of the anti-Stokes N2 PRR J=6 channel for the adjacent O_2 and N_2 lines. As seen in Fig. 3(a), the J=6 channel (IF1) plus FPI1) can generate a suppression of more than 2 orders of magnitude to the adjacent anti-Stokes O_2 PRR J=7 and J=9 lines (the Raman-shifted wavelength = 531.181 and 530.857 nm) as well as anti-Stokes N_2 PRR J=5 and J=7 lines (the Raman-shifted wavelength = 530.776 and 531.225 nm). This indicates that the J = 6 channel can effectively extract the single anti-Stokes N_2 PRR J = 6 line.

The FPI2 adjustment was accomplished under the condition that the output wavelength of the dye laser was set to the anti-Stokes N_2 PRR J=16 line (528.770 nm). The normalized PMT2 signal intensity was also estimated in the same way as above for the laser emissions at the anti-Stokes N_2 PRR J=16 line and the four O_2 and O_2 lines close to it (see Fig. 3(b)). The J=16 channel (IF2 plus FPI2) invokes a suppression of ~2 orders of magnitude to the adjacent anti-Stokes O_2 PRR J=21 and J=23 lines (the Raman-shifted wavelength = 528.928 and 528.609 nm) as well as anti-Stokes O_2 PRR O_2 PRR O_3 lines (the Raman-shifted wavelength = 528.992 and 528.549 nm). Therefore, the anti-Stokes O_3 PRR O_3 PRR O_3 lines (the Raman-shifted wavelength = 528.992 and 528.549 nm). Therefore, the anti-Stokes O_3 PRR O_3 PRR O_3 lines in the two PRR channels indicate that the current PRR lidar is actually a single-line-extracted system.

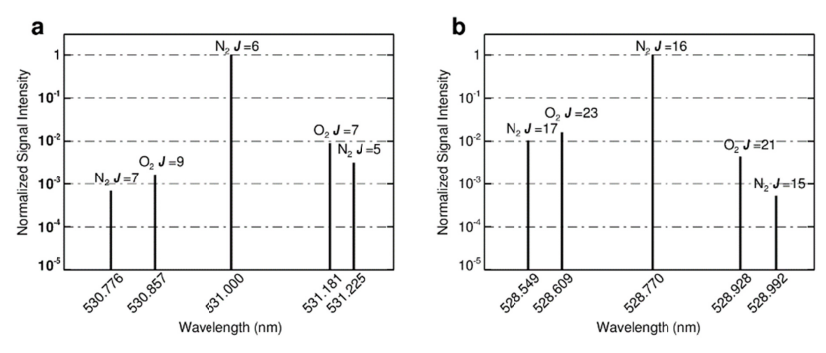


Fig. 3. a. Normalized PMT1 signal intensity for the laser emissions at the anti-Stokes N_2 PRR J=6 line and the four O_2 and N_2 lines close to it. The normalization factor is the signal intensity value at the anti-Stokes N_2 PRR J=6 line. b. Same as Fig. 3(a), except for the PMT2 in the anti-Stokes N_2 PRR J=16 line channel. Note that the lowest suppression value of the PRR channels to the adjacent O_2 and N_2 lines is 0.0161 (for the anti-Stokes O_2 PRR J=23 line).

Based on the PMT1 and PMT2 signal intensities obtained for the dye laser emissions at the anti-Stokes N_2 PRR J=6 and J=16 lines (elastic backscatter signals measured at the J=6 and J=16 channels), we can evaluate the parameter b. Figure 4 presents the natural logarithm of the signal intensity ratio $N_{\nu_0=\nu_{J=16}}(z)/N_{\nu_0=\nu_{J=6}}(z)$ as a function of altitude. Each signal represents a time-integration over one minute. The plotted altitude range (2.5-5.0 km) was set by jointly considering the signal-to-noise ratio and overlap geometry between the laser beam and telescope. The natural logarithm of the signal intensity ratio shows small fluctuation in altitude that is due to the statistical uncertainty of the photon counting signals. In light of the Eq. (10), the average signal ratio is equivalent to the ratio of the system factors $C_{\nu_0=\nu_{J=16}}$ / $C_{\nu_0=\nu_{J=6}}$ given a fact that the backscatter and extinction coefficients (due to both aerosol particles and air molecules) at frequency $v_{J=6}$ closely approach those at frequency $v_{J=16}$. As mentioned above, each system factor is proportional to the transmitted laser pulse energy and the overall channel efficiency. In terms of our measurement, the dye laser had nearly the same pulse energy (~6 mJ) at the two emission wavelengths. Then the ratio $C_{\nu_0=\nu_{J=16}}$ / $C_{\nu_0=\nu_{J=6}}$ reduces to the ratio of the channel efficiency in the anti-Stokes N_2 PRR J=16 and J=6 channels, that is equivalent to the ratio $C_{J=16} \ / \ C_{J=6}$. Therefore the natural logarithm of the channel efficiency ratio $\ln \left(C_{J=16} / C_{J=6} \right)$ has a value of 1.03 (see Fig. 4). Inserting this value into Eq. (9), we have b = 2.07. The theoretical/measured results of a and b provide a standard for the parameter calibration in the case of the single-line-extracted PRR lidar.

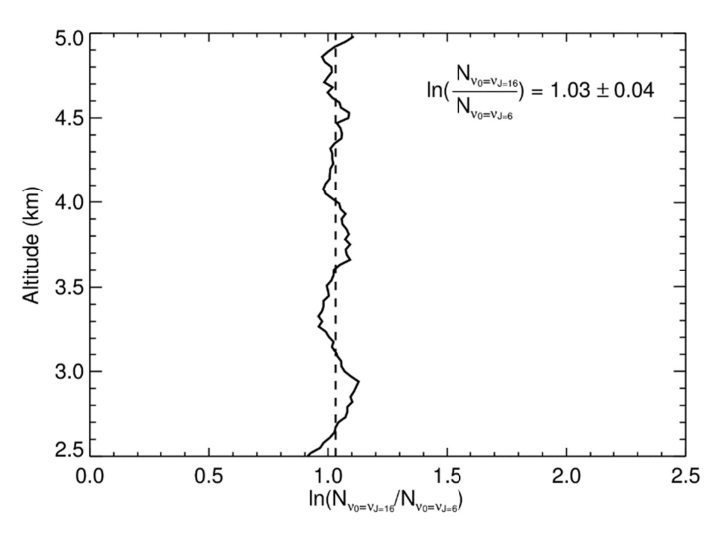


Fig. 4. Natural logarithm (solid curve) of the ratio of the 1-min-integrated signal intensity at the J=16 and J=6 channels as a function of altitudes when the dye laser was tuned to the anti-Stokes N_2 PRR J=16 line (528.770nm) and J=6 line (531.000 nm) respectively. The plotted altitude range (2.5-5.0 km) was set by considering the signal-to-noise ratio and overlap geometry between the laser beam and telescope. The signal intensity ratio shows small fluctuation in altitude that is due to the statistical uncertainty of the photon counting signals. Its average is equivalent to the channel efficiency ratio $C_{J=16} / C_{J=6}$ in the anti-Stokes N_2 PRR J=16 and J=6 channels.

According to the conventional lidar calibration method [2,4,5,7], the constant parameters a and b were also derived via comparison with accompanying radiosondes launched at 2000 LT from Wuhan Weather Station (~23.4 km away from our lidar site). The utilized lidar data were integrated over 60 min. In order to avoid the impact of the overlap factor at the lower altitudes and weak signal-to-noise ratio at high altitudes, the calibration of the parameters a and b was made in an altitude range from 2.0 to 8.0 km. Figure 5 presents the natural logarithm of the signal ratio (of the two PRR channels) $\ln Q(T)$ versus the reciprocal of accompanying radiosonde temperature 1/T for four different observation nights. According to our calculations, the $1-\sigma$ standard deviations of the two constants (a and b) are quite small (both the relative standard deviations are less than 3%), indicating the stability of the single-line-extracted PRR lidar. The a calibration value (-660.01 ± 5.80 K) is very close to the theoretical result (-658.38 K) from Eq. (8) with a relative deviation of 0.2%, while the b calibration value (2.00 ± 0.06) closely approaches the measured value (2.07) with a relative deviation of 3.5%. This reconfirms that the current PRR lidar is a single-line-extracted lidar system.

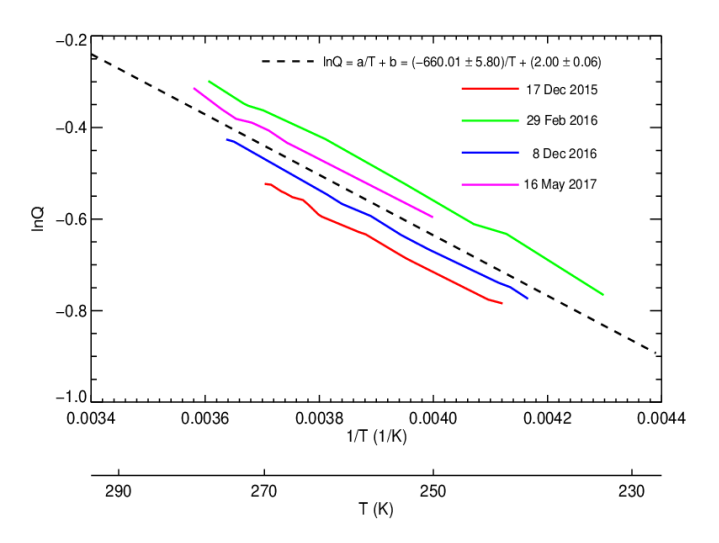


Fig. 5. Natural logarithm of the signal ratio (of the two PRR channels) versus the reciprocal of accompanying radiosonde temperature for four different observation nights. The lidar data were integrated over 60 min. The calibration of the constants a and b was made in an altitude range from 2.0 to 8.0 km. The dashed line is a best fit through the data from the four calibration days.

5. Observational examples

The measurement examples shown in this section were obtained at our atmospheric observation site on the campus of Wuhan University in Wuhan (30.5°N, 114.4°E), China. Figure 6 exhibits a temperature profile (red) measured by the single-line-extracted PRR lidar during 1930-2029 LT on 16 December 2016 and the temperature profile (black) from an accompanying radiosonde (launched at 2000 LT on the same day from Wuhan Weather Station). The lidar temperature profile has a range resolution of 150 m. As seen in Fig. 6, the lidar temperature matched the radiosonde data very well in the 1.0-6.5 km altitude range with an absolute deviation less than 1 K (Fig. 6(b)). A deviation of ~1-3.4 K at altitudes of 6.5-10.0 km might arise from radiosonde drift-off or low lidar signal-to-noise ratio. The 1- σ statistical uncertainty of the lidar temperature measurement is below 1 K up to ~7.7 km (below 0.5 K up to 4.2 km). Figure 7 shows the lidar and radiosonde temperature profiles measured under daytime conditions. The statistical uncertainty for the lidar measurement is less than 1 K up to ~3.9 km, while the temperature deviations between the lidar and radiosonde do not exceed 1 K at altitudes below 3.7 km (a deviation of ~1.6 K around 1.2 km might arise from the 23-km distance between lidar site and radiosonde). Figure 8 gives timeheight contour of the atmospheric temperature measured by the single-line-extracted PRR lidar on 11 January 2018. A sliding average of 60 minutes was applied to the lidar data with resolutions of 1 min and 30 m. The single-line-extracted PRR lidar has an all-day temperature measurement capability. At daytime the lidar temperature measurement extended up to ~2.6 km with the RMS deviation and statistical uncertainty both not exceeding 1 K. As seen in Fig. 8, the temperature at lower altitudes showed a typical evolution of the boundary layer style over land on a sunny day [20]. Therefore the single-line-extracted PRR lidar allows us to study the behavior of the convective boundary layer.

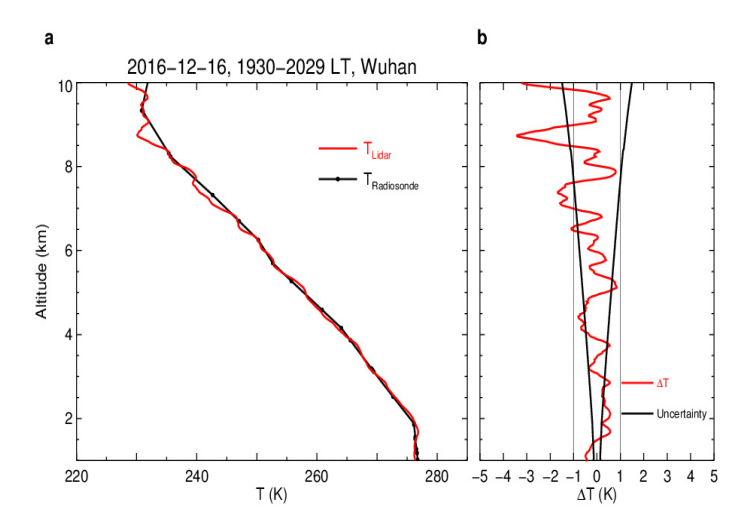


Fig. 6. a. Temperature profile (red) measured with the single-line-extracted PRR lidar during 1930-2029 LT on 16 December 2016. The range resolution is 150 m. Temperature data (black) from a radiosonde launched from Wuhan Weather Station (~23.4 km away from our lidar site) at 2000 LT are shown for comparison. b. Deviation between the lidar and radiosonde temperature profiles (red) and the $_{1-\sigma}$ statistical uncertainty of the lidar temperature measurement (black). The statistical uncertainty is less than 1 K up to ~7.7 km, while the deviations for this measurement do not exceed 1 K at altitudes below 6.5 km.

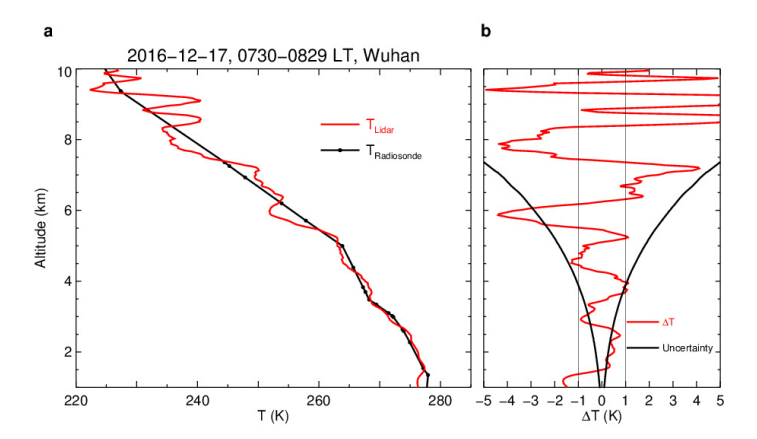


Fig. 7. **a.** Temperature profile (red) measured with the single-line-extracted PRR lidar during 0730-0829 LT on 17 December 2016. The range resolution is 150 m. Temperature data (black) from a radiosonde launched from Wuhan Weather Station (\sim 23.4 km away from our lidar site) at 2000 LT are shown for comparison. **b.** Deviation between the lidar and radiosonde temperature profiles (red) and the $_{1-\sigma}$ statistical uncertainty of the lidar temperature measurement (black). The statistical uncertainty is less than 1 K up to \sim 3.9 km, while the deviations for this measurement do not exceed 1 K at altitudes below 3.7 km (a deviation of \sim 1.6 K around 1.2 km arose from the 23-km distance between lidar site and radiosonde).

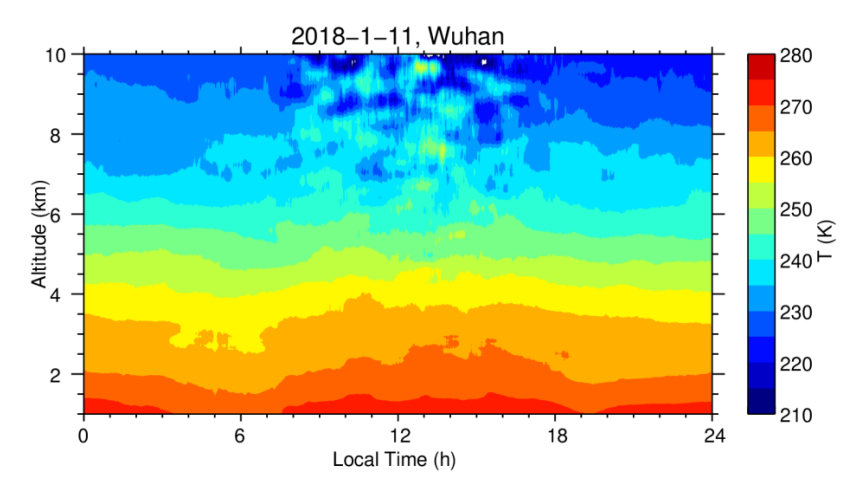


Fig. 8. Time-height contour plot of all-day temperature measured by the single-line-extracted PRR lidar on 11 January 2018. A sliding average of 60 minutes was applied to the lidar data with resolutions of 1 min and 30 m. The daytime temperature measurement could extend up to 2.6 km. Note that the temperature at lower altitudes showed a typical evolution of the boundary layer over land on a sunny day.

Figure 9 shows the time-height contour of the lidar-measured backscatter ratio on 11 January 2018 (the same date as in Fig. 8). On this day, most aerosol particles were present at altitudes below ~2.5 km (in the boundary layer). They represented locally-generated aerosol (urban aerosol) layer. Figure 10 gives the mean profiles of the atmospheric temperature and particle optical properties during 0700-0800 LT on this day. The urban aerosol layer peaked at ~1.6 km with a backscatter ratio of R = 2.7 and particle extinction coefficient of $\alpha_a = 0.15$ km⁻¹. The urban aerosol layer had a temporary lidar ratio of ~63 sr and a volume depolarization ratio of ~0.07 (measured with a co-located polarization lidar at 532 nm). The magnitudes of the aerosol optical properties represent a mild pollution episode.

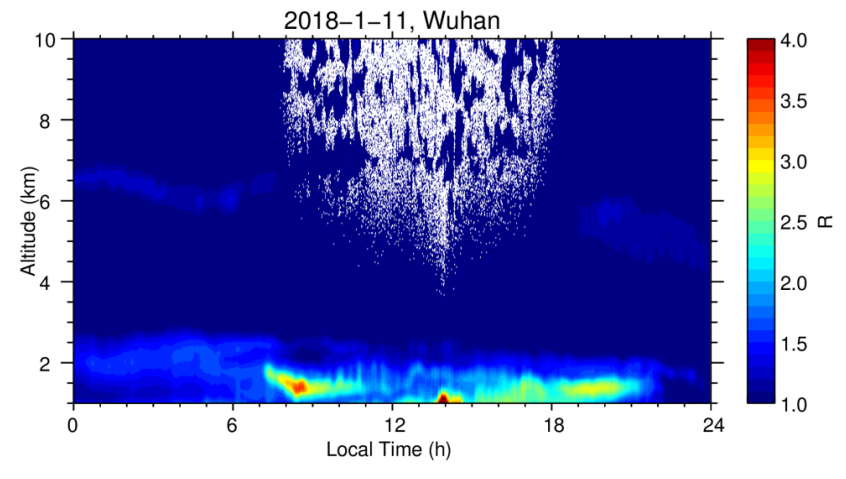


Fig. 9. Time-height contour plot of backscatter ratio measured by the single-line-extracted PRR lidar on 11 January 2018. A sliding average of 60 minutes was applied to the lidar data with resolutions of 1 min and 30 m.

Figure 11 plots the mean profiles of the atmospheric temperature and particle optical properties measured by the single-line-extracted PRR lidar during 2000-2100 LT on 12 April 2017, that represent an example of dust layers. The dust layer occurred at altitudes of 2.4-4.5 km with a peak depolarization ratio of ~0.24 and peak backscatter ratio of ~3.6. The

calculated layer lidar ratio exhibits a small altitude variation ranging from \sim 39 to 48 sr. The radiosonde data at \sim 2000 LT from Wuhan Weather Station indicate a moderate relative humidity (42-50%) on the layer. Dust layers were identified on 10 occasions from 58 observation days with the single-line-extracted PRR lidar. Interestingly, their lidar ratio values were 47 \pm 8 sr which might represent a feature of dust layers observed in the free troposphere at middle and low latitudes.

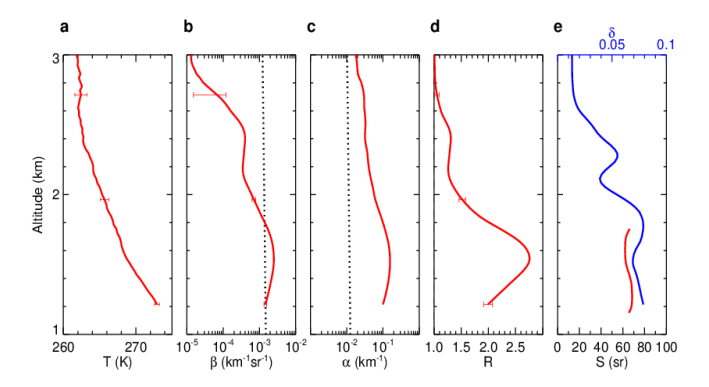


Fig. 10. Profiles of **a.** temperature T, **b.** particle backscatter coefficient β_{\perp} , **c.** particle extinction coefficient α_{\perp} , **d.** backscatter ratio R and **e.** lidar ratio S measured by the single-line-extracted PRR lidar during 0700-0800 LT on 11 January 2018, which exhibit a mild example of urban aerosol layers. The molecular backscatter and extinction coefficients are also plotted by black dotted line. The depolarization ratio S profile measured with a co-located polarization lidar at 532 nm is also plotted. Error bar denotes the uncertainty induced by signal noise

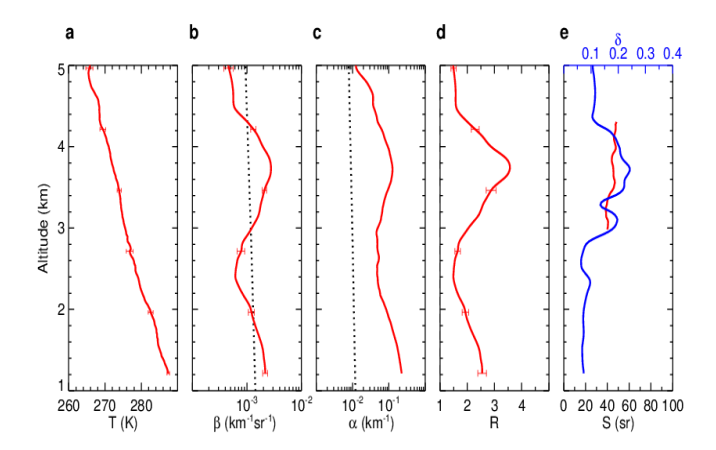


Fig. 11. Profiles of **a.** temperature T, **b.** particle backscatter coefficient β_{*} , **c.** particle extinction coefficient α_{*} , **d.** backscatter ratio R and **e.** lidar ratio S measured by the single-line-extracted PRR lidar during 2000-2100 LT on 12 April 2017. which exhibit an example of dust layers. A relative humidity of ~42-50% was observed on the layer by an accompanying local radiosonde at 2000 LT. The molecular backscatter and extinction coefficients are also plotted by black dotted line. The depolarization ratio δ profile measured with a co-located polarization lidar at 532 nm is also plotted. Error bar denotes the uncertainty induced by signal noise.

Figure 12 shows an example of cirrus clouds observed by the single-line-extracted PRR lidar during 2300-2359 LT on 13 May 2017. The cirrus layer extended from ~7.8 to 12.9 km.

On the cirrus bottom (7.8–9.3 km), the backscatter ratio showed a prominent peak ($R \sim 53$ at 8.7 km), while both the lidar ratio and depolarization ratio took their minimum values (S = 1.1 sr and $\delta = 0.03$) around the peak altitude, indicating a horizontally-oriented ice crystals [21, 22]. On the upper part of the cirrus layer (9.3–12.9 km), the backscatter ratio values ranged between 5 and 18 sr, while the values of the lidar ratio and depolarization ratio were respectively 10–21 sr and 0.23–0.44. The observed results suggest that the upper part of the cirrus layer consists of randomly oriented ice crystals. Seven cirrus events were recognized from the 58-day lidar measurements. They yielded a mean lidar ratio of 17 ± 5 sr and a mean depolarization ratio of more than 0.23 ± 0.13 for the randomly oriented ice crystals, whereas the corresponding values were 1.7 ± 0.9 sr and 0.016 ± 0.007 for horizontally-oriented ice crystals.

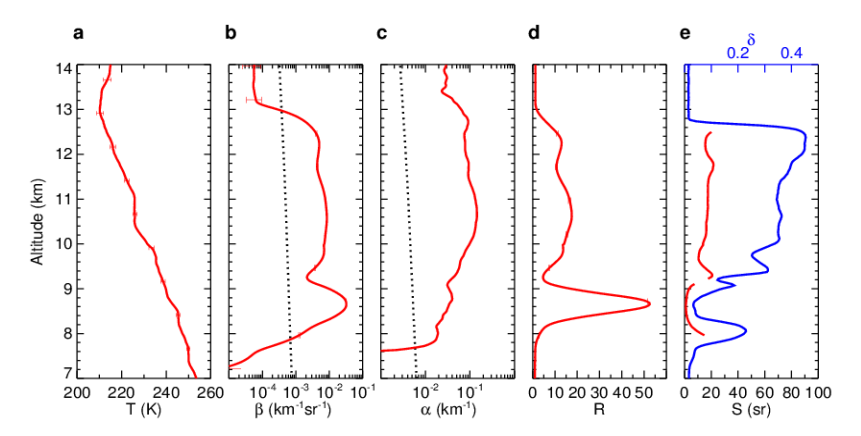


Fig. 12. Profiles of **a.** temperature T, **b.** particle backscatter coefficient β_a , **c.** particle extinction coefficient α_a , **d.** backscatter ratio R and **e.** lidar ratio S measured by the single-line-extracted PRR lidar during 2300-2359 LT on 13 May 2017, which exhibit an example of cirrus. The molecular backscatter and extinction coefficients are also plotted by black dotted line. The depolarization ratio S profile measured with a co-located polarization lidar at 532 nm is also plotted. Error bar denotes the uncertainty induced by signal noise.

6. Summary and conclusion

We have built the first single-line-extracted pure rotational Raman (PRR) lidar that effectively detects two isolated N_2 molecule PRR line signals (anti-Stokes PRR lines J=6 and 16) as well as elastic backscatter signal. The lidar transmitter is an injection-seeded frequency-doubled Nd:YAG laser (532.237 nm) with a pulse energy of ~800 mJ and a repetition rate of 30 Hz. The receiver utilizes a 200-mm Cassegrain telescope. The combined interference filter and Fabry-Perot interferometer are used to extract desired N_2 molecule PRR line signal, and suppress adjacent O_2 molecule line signals as well as strong elastic signal in each PRR channel. The elastic signal is extracted by an interference filter with a 0.3-nm bandwidth and ~80% peak transmission at 532.237 nm.

This lidar system enables all-day temperature profiles to be obtained strictly according to the simple two-parameter functional relation (the most basic principle of the PRR temperature lidar) between temperature and ratio of the two PRR line signals. One parameter a is a known constant which depends only on the difference of the rotational Raman energies of the two extracted lines, while another b can be obtained by measuring the ratio of the overall efficiencies in the two N_2 PRR line channels. Hence the single-line-extracted PRR lidar allows the atmospheric temperature measurements without calibration from reference temperature data (e.g., radiosonde temperature). The parameters a and b were obtained also

via comparison with accompanying local radiosondes. The calibrated a and b values are very close to the theoretical and measured results with respective relative deviations of 0.2% and 3.5%. The perfect agreement validates that our PRR lidar is a single-line-extracted lidar system.

Combining the lidar equations for one single-line-extracted PRR signal and elastic signal, we have derived a new analytical expression of the particle backscatter coefficient (or backscatter ratio). It is indicated that the particle backscatter coefficient (or backscatter ratio) can be determined simply from the signal profiles measured in one single-line extracted PRR channel and elastic channel as well as the lidar temperature profile without additional assumptions (e.g. lidar ratio or Ångström relationship). The particle extinction coefficient is derived further from the acquired particle backscatter coefficient profile and elastic signal profile. The lidar ratio can be obtained then from the derived particle extinction coefficient and backscatter coefficient. The two particle optical parameters as well as resultant lidar ratio provide quantitatively strict standards for the lidar measurements of aerosol and cloud.

Observational examples show the capability for the current lidar to measure all-day atmospheric temperature profiles and aerosol/cloud optical properties. For an altitude resolution of 150 m and a time resolution of 60 min, the temperature measurement altitude at nighttime reached ~6.5 km with the RMS deviation between the lidar and concurrent radiosonde and the statistical uncertainty both being better than 1 K. At daytime the lidar temperature measurement extended up to ~2.6 km with the RMS deviation and statistical uncertainty both not exceeding 1 K. An observational example of all-day time-altitude contour of the lidar-measured temperature is presented. It is observed that the temperature at lower altitudes showed a typical evolution of the boundary layer style over land on a sunny day. Based on the strict analytical expressions derived from the lidar equations for the single-line-extracted PRR channel and elastic channel, the optical properties of the urban aerosol, dust layer and cirrus clouds were obtained.

Funding

National Natural Science Foundation of China (NSFC) (41521063, 41327801); Meridian Space Weather Monitoring Project (China).

References

- Y. Arshinov, S. Bobrovnikov, I. Serikov, A. Ansmann, U. Wandinger, D. Althausen, I. Mattis, and D. Müller, "Daytime operation of a pure rotational Raman lidar by use of a Fabry-Perot interferometer," Appl. Opt. 44(17), 3593–3603 (2005).
- I. Balin, I. Serikov, S. Bobrovnikov, V. Simeonov, B. Calpini, Y. Arshinov, and H. van den Bergh, "Simultaneous measurement of atmospheric temperature, humidity, and aerosol extinction and backscatter coefficients by a combined vibrational pure-rotational Raman lidar," Appl. Phys. B 79(6), 775–782 (2004).
- A. Behrendt, T. Nakamura, M. Onishi, R. Baumgart, and T. Tsuda, "Combined Raman lidar for the measurement
 of atmospheric temperature, water vapor, particle extinction coefficient, and particle backscatter coefficient,"
 Appl. Opt. 41(36), 7657–7666 (2002).
- 4. P. Di Girolamo, "Rotational Raman Lidar measurements of atmospheric temperature in the UV," Geophys. Res. Lett. **31**(1), L01106 (2004).
- 5. J. Jia and F. Yi, "Atmospheric temperature measurements at altitudes of 5-30 km with a double-grating-based pure rotational Raman lidar," Appl. Opt. **53**(24), 5330–5343 (2014).
- 6. M. Radlach, A. Behrendt, and V. Wulfmeyer, "Scanning rotational Raman lidar at 355 nm for the measurement of tropospheric temperature fields," Atmos. Chem. Phys. 8(2), 159–169 (2008).
- A. Behrendt, "Temperature Measurements with Lidar," in Lidar Range-Resolved Optical Remote Sensing of the Atmosphere, C. Weikamp, ed. (Springer, 2005), pp. 273–305.
- A. Ansmann, M. Tesche, P. Seifert, D. Althausen, R. Engelmann, J. Fruntke, U. Wandinger, I. Mattis, and D. Müller, "Evolution of the ice phase in tropical altocumulus: SAMUM lidar observations over Cape Verde," J. Geophys. Res. 114(D17), D17208 (2009).
- D. S. Balis, V. Amiridis, S. Nickovic, A. Papayannis, and C. Zerefos, "Optical properties of Saharan dust layers as detected by a Raman lidar at Thessaloniki, Greece," Geophys. Res. Lett. 31(13), L13104 (2004).
- P. Cottle, K. Strawbridge, I. McKendry, N. O'Neill, and A. Saha, "A pervasive and persistent Asian dust event over North America during spring 2010: lidar and sunphotometer observations," Atmos. Chem. Phys. 13(9), 4515–4527 (2013).

- A. Hänel, H. Baars, D. Althausen, A. Ansmann, R. Engelmann, and J. Y. Sun, "One-year aerosol profiling with EUCAARI Raman lidar at Shangdianzi GAW station: Beijing plume and seasonal variations," J. Geophys. Res. Atmos. 117(D13), D13201 (2012).
- 12. Z. Liu, A. Omar, M. Vaughan, J. Hair, C. Kittaka, Y. Hu, K. Powell, C. Trepte, D. Winker, C. Hostetler, R. Ferrare, and R. Pierce, "CALIPSO lidar observations of the optical properties of Saharan dust: A case study of long-range transport," J. Geophys. Res. 113(D7), D07207 (2008).
- 13. C. Wu and F. Yi, "Local ice formation via liquid water growth in slowly ascending humid aerosol/liquid water layers observed with ground-based lidars and radiosondes," J. Geophys. Res. Atmos. 122(8), 4479–4493 (2017).
- 14. F. G. Fernald, "Analysis of atmospheric lidar observations: some comments," Appl. Opt. 23(5), 652–653 (1984).
- 15. A. Ansmann and D. Müller, "Lidar and Atmospheric Aerosol Particles," in *Lidar Range-Resolved Optical Remote Sensing of the Atmosphere*, C. Weikamp, ed. (Springer, 2005), pp. 105–141.
- U. Wandinger, "Raman Lidar," in Lidar Range-Resolved Optical Remote Sensing of the Atmosphere, C. Weikamp, ed. (Springer, 2005), pp. 241–271.
- A. Behrendt and J. Reichardt, "Atmospheric temperature profiling in the presence of clouds with a pure rotational Raman lidar by use of an interference-filter-based polychromator," Appl. Opt. 39(9), 1372–1378 (2000).
- 18. V. Matthais, V. Freudenthaler, A. Amodeo, I. Balin, D. Balis, J. Bösenberg, A. Chaikovsky, G. Chourdakis, A. Comeron, A. Delaval, F. De Tomasi, R. Eixmann, A. Hågård, L. Komguem, S. Kreipl, R. Matthey, V. Rizi, J. A. Rodrigues, U. Wandinger, and X. Wang, "Aerosol lidar intercomparison in the framework of the EARLINET project. 1. Instruments," Appl. Opt. 43(4), 961–976 (2004).
- A. Behrendt, T. Nakamura, and T. Tsuda, "Combined temperature lidar for measurements in the troposphere, stratosphere, and mesosphere," Appl. Opt. 43(14), 2930–2939 (2004).
- D. Cimini, F. De Angelis, J.-C. Dupont, S. Pal, and M. Haeffelin, "Mixing layer height retrievals by multichannel microwave radiometer observations," Atmos. Meas. Tech. 6(11), 2941–2951 (2013).
- A. Ansmann, "Ice formation in Saharan dust over central Europe observed with temperature/humidity/aerosol Raman lidar," J. Geophys. Res. 110, D18S12 (2005).
- V. Noel and K. Sassen, "Study of ice crystals orientation in ice clouds based on polarized observations from the fars scanning lidar," in 22nd International Laser Radar Conference, G. Pappalardo and A. Amodeo, (2004), pp. 309–312.